Engineering Efficient Light Sources for Silicon Photonics: III-V Nano-heterostructures Monolithically Grown on Silicon

Alisha Nanwani[1,2,*], Paweł Wyborski[1,3], Michael S. Seifner[2,4], Shima Kadkhodazadeh[2,4], Grzegorz Sęk[3], Paweł Holewa[1,2,3,**], Kresten Yvind[1,2], Elizaveta Semenova[1,2]

[1]Department of Electrical and Photonics Engineering, Technical University of Denmark, Denmark

[2]Nanophoton- Centre for Nanophotonics, Technical University of Denmark, Denmark

[3]Department of Experimental Physics, Faculty of Fundamental Problems of Technology, Wrocław University of Science and Technology, 50-370 Wrocław, Poland

[4]DTU Nanolab, Technical University of Denmark, Denmark

*atana@dtu.dk, **pawhol@dtu.dk

The demand for advanced photonics technology is increasing rapidly, fueled by the necessity for high-performance and cost-effective optical information processing systems extending into the quantum domain. Silicon, benefiting from its mature fabrication processes, stands as an ideal platform. However, its inherent indirect bandgap leads to inefficient light emission. To overcome this drawback, the integration of III-V materials has proven essential. These materials are recognized for their efficient light emission and superior bandgap engineering capabilities, making them indispensable in photonics and beyond. Here, we present the monolithic integration of small-volume III-V nano-heterostructures with silicon via selective area epitaxy in the pyramidal openings etched in (100)-oriented silicon substrate. The precise positioning of the nano-heterostructures is achieved using electron beam lithography. Our atomic resolution imaging and chemical analysis confirm the epitaxial nature of InP growth, revealing well-defined heterointerfaces. Each structure incorporates an InAsP quantum dot-like active medium. Optical characterization and eight-band k·p calculations demonstrate energy level quantization in three spatial dimensions. The heterostructures can be engineered to cover the entire telecom wavelength range. Consequently, these InAsP/InP nano-heterostructures could serve as a gain medium for silicon-based hybrid nano-lases and nanoLED as well as quantum light sources in the telecom wavelength range.

Introduction

Integrating III-V active material with silicon platform has been a longstanding goal, leveraging the advantages of a well-established and cost-effective silicon photonic platform with addition of active photonic devices such as light sources and detectors, [1,2].In the past two decades, III-V/Si heterogeneous integration through bonding techniques has gained academic and commercial recognition as a promising path towards realization of on-chip light sources [3–6]. With the rapid advancements in the field of silicon-based integrated photonics for applications in artificial intelligence, hyper-scale data centers, high-performance computing, light detection and ranging (LIDAR)[7], monolithically integrated light sources are in high demand. The realization of a reliable method of monolithic integration of III-V compound semiconductor heterostructures onto host silicon-photonic circuits not only allows for higher integration density[8] but will

also significantly simplify the technological process. Moreover, a reduction in power consumption of III-V materials will have a positive environmental impact.

Monolithic integration of III-V compound semiconductors into silicon via direct epitaxial growth has been extensively investigated for a few decades, with considerable progress occurring in recent years[9–17]. Various methods are actively explored in this respect, including the use of thick buffer layers[18–20], selective area growth (SAG) technique[21–26], the growth of nanostructures using droplets of metals as catalysts[27–29,] and a combination of SAG and metal droplet mediated approach[30]. However, emitters fabricated using thick buffer layers can suffer from coupling issues with passive waveguides and recently some research groups have tried resolving this issue by etching the entire box layer and regrowing thick buffers to compensate for the box thickness[31]. Therefore, the latter three approaches are more promising due to their flexible integration into Si-based circuits, avoiding the use of expensive III-V substrates and wafer bonding process, as well as difficulties with the alignment of III-V elements with the Si-circuit.

Benefiting from high-quality III-V material growth obtained using these methods, various silicon-based laser structures have been demonstrated with outstanding performance[22,24,32,33]. SAG has emerged as a viable alternative, enabling precise positioning[24,34–36] of nanostructures with reduced defect densities due to a smaller footprint resulting in smaller nucleation area compared to the planar growth[35], and close to thermodynamic equilibrium growth conditions[27,29,37,38]. The accurate alignment of the active III-V material with other photonic or electronic circuit layers is an enabling step for optoelectronic applications such as photonic cavities, nanolasers, or nano-LEDs.

Here, we demonstrate the realization of $InP/InAs_xP_{1-x}/InP$ nano-heterostructures of a few tens of nm, monolithically grown on silicon and emitting in the telecom wavelengths range. Silicon wafers with (100) orientation were patterned with an array of inverted pyramidal holes confined by the {111} family of planes to grow III-V nano-heterostructures via metalorganic vapor phase epitaxy (MOVPE) using the SAG approach. We examine the controllability of the emission wavelength of the III-V nano-heterostructures by varying the arsenic content in the $InAs_xP_{1-x}$ region, exploring the potential applications of III-V nanostructures in silicon-based photonic devices. The nanostructures are investigated in the scanning transmission electron microscope (STEM), revealing the geometry and composition of the InAsP quantum dot (QD)-like structures. The optical properties of nano-heterostructures are investigated by cryogenic micro-photoluminescence (μPL) and time-resolved photoluminescence (TRPL) setup. The results suggest that the nanostructures are characterized by the QD-like three-dimensional (3D) quantum confinement, further confirmed by the eight-band $k{\cdot}p$ calculations.

The proposed method of synthesizing $InP/InAs_xP_{1-x}/InP$ nano-heterostructures on silicon by SAG is prospective for the realization of efficient light emitters on silicon-based platform covering the second and third telecom wavelength windows. Consequently, this study contributes to ongoing efforts to advance the silicon-on-insulator platforms via

integration of III-V compound semiconductor material for next-generation optoelectronic devices compatible to CMOS processing[31].

Results and discussion

Epitaxial growth of III-V nano-heterostructures on silicon

Undoped silicon (001) wafers are used as a growth substrate for SAG, with e-beam patterned nano-sized openings varying in size from 20 to 50 nm. The pattern is transferred from a Si_3N_4 hard mask into the Si wafer by KOH etching, forming inverted pyramidal holes confined by the {111} family of planes[30]. The InP/$InAs_xP_{1-x}$/InP nano-heterostructures are grown by the SAG method using a low-pressure (60 Torr) reactor. Ultra-high purity hydrogen (H_2) is used as a carrier gas and trimethyl-indium (TMIn), phosphine (PH_3), arsine (AsH_3) and tertiary-butyl-phosphine (TBP) are the growth precursors (see Methods for description of the sample preparation and growth process). Figure 1a schematically illustrates the growth process, while Figs. 1b-d show side and top views of the resulting nano-heterostructure with $InAs_xP_{1-x}$ QD.

First, site-selective growth of an InP seed is optimized for different growth durations (40-110 s) at 600 °C with a molar flow ratio for the group V and III materials (V/III ratio) of 1690, with TMIn flux of 5.28×10^{-6} mol/min and PH_3 flux of 8.92×10^{-3} mol/min. InP growth time of 40 s was sufficient to fill the openings so that the active material is in-plane with the Si-circuit and also enough to trap the defects parallel to (111) planes at the Si_3N_4 undercut region. TMIn and PH_3 flows were paused for the QD-like structure formation, while AsH_3 was turned on to promote the As/P exchange. As a result, the nano-heterostructures were synthesized with interfaces oriented along (001) direction which are shown in STEM images (Fig.2).

Table 1. summarizes the growth parameters used for three exemplary samples, S-1, S-2, and S-3. For sample S-1, the formation of the $InAs_xP_{1-x}$ layer was initiated by a 5-minute-long arsine exposure at 510 °C on an as-grown InP seed. It was subsequently capped with InP at V/III = 607 at the same temperature. The PL emission wavelength for this structure at low temperature (5 K) is 1240 nm. Extending the arsine exposure to 7 min led to increased surface irregularities on the InP cap, indicative of defective growth, which was also observed in Ref. 39 with increased duration of As/P exchange. Consequently, instead of prolonging the arsine exposure, we increased the arsenic flux from 2.38×10^{-3} mol/min to 7.81×10^{-3} mol/min to redshift the emission wavelength to the C-band. This, however, resulted in a lack of further emission wavelength shift. This could be due to the limited effectiveness of As/P exchange on different facets as shown in Ref. 39.

Sample ID	Growth time for InP seed	Annealing in PH_3 flux	As/P exchange duration	AsH_3 Flux [mmol/min]	InP cap growth	Emission wavelength
S-1	40 s	0 s	300 s	2.23	20 s	1240 nm
S-2	110 s	800 s	180 s	7.81	20 s	1420 nm
S-3	110 s	800 s	300 s	7.81	20 s	1620 nm

Table 1. Comparison of the growth parameters and PL emission wavelength for investigated samples.

To promote formation of multiple facets on the InP seed, we increased the growth duration to 110 s to overgrow the mask level, followed by annealing in PH_3 ambient for approximately 15 mins. Annealing promotes the formation of multiple facets on the InP seed during its initial desorption phase, reducing its thickness to the same seed thickness as S-1 and regulates the defect count[30]. As/P exchange was then conducted for 3 mins (S-2) and 5 mins (S-3) at high arsenic fluxes, as shown in Table 1. We expect variations in thickness and composition of the $InAs_xP_{1-x}$ layer on the different crystallographic planes, depending on the effectiveness of the As/P exchange for each facet. A long As/P exchange duration of 5 minutes results in an InAsP layer above pseudomorphic critical thickness that can be identified by a defective InP cap layer in S-3 (not shown here). The strain in the InAsP layer releases via the formation of dislocations propagating in the InP cap layer as also shown in Ref. 38, which result in the promotion of non-radiative carrier recombination channels.

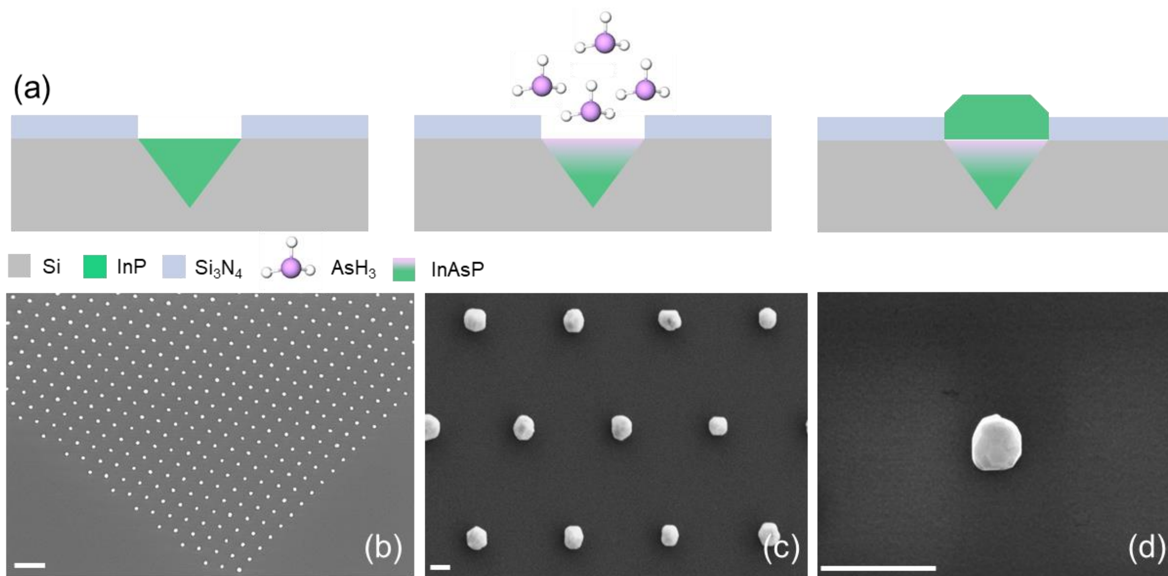

Figure 1. Epitaxy of nano-heterostructures with InAsP quantum dot-like structure. (a) Schematic illustration of the growth procedure on silicon: the opening in Si is filled with the InP seed (left), the As/P exchange is performed in As-ambient (center), the InAsP nano-heterostructure is capped with InP, (b) 30×30 μm array of InAsP/InP nano-heterostructures grown, scale bar: 2 μm, (c) InP cap of the nano-heterostructures grown in 20 nm-size openings, scale bar: 200 nm, (d) a single 50 nm opening filled with a nano-heterostructure, scale bar: 50 nm.

Atomic-scale investigation of QD-like nano-heterostructures

Figure 2a shows dark-field (HAADF) STEM image of an InP/InAsP/InP nano-heterostructure with an approximate opening size of 50 nm for sample S-2. Images and chemical analysis data for samples S-1 and S-3 are shown in Supplementary Fig. 1. High magnification STEM images of the As-containing heterostructure and Si/InP interface are shown in Figs. 2b and 2c, respectively. Figure 2c shows an atomically sharp interface between Si and InP at the {111} boundaries of the etched pyramids. The InAsP/InP QD-like structure can be clearly observed in Figure 2b and is confirmed by the EDS chemical composition maps shown in Figure 2e-g. The InAsP region has a thickness of 12 nm, and it is sandwiched between the InP seed and cap layers.

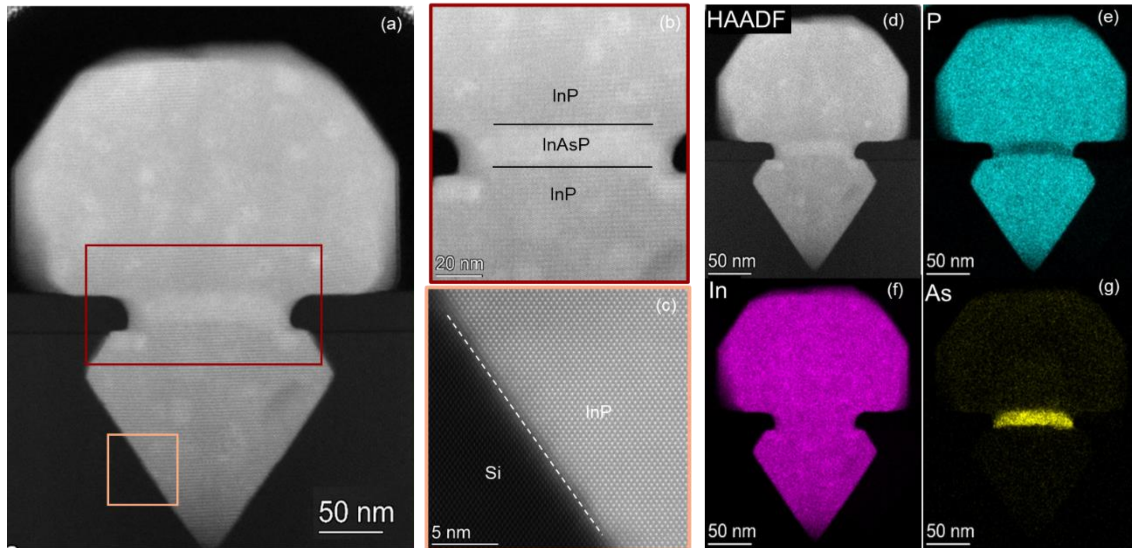

Figure 2. STEM images of the InAsP QD-like nanostructure embedded in InP epitaxially grown on silicon for sample S-2. (a) STEM image of the nanostructure, (b), (c) the high-magnification images around the (b) InAsP region with 12 nm thickness, (c) Atomic structure image of the hetero-interface region between Si and InP. (d)-(g) EDS analysis of InAsP/InP nano-heterostructure: (d) HAADF-STEM image, and (e-g) 2D elemental maps by EDS of (e) P (cyan), (f) In (magenta), and (g) As (yellow), respectively.

Figure 2d-g presents the HAADF-STEM image and the corresponding material distribution of P (Fig. 2e, cyan), In (Fig. 2f, magenta), and As (Fig. 2g, yellow) along the heterointerface. It can be clearly seen that the distribution of In is uniform across the entire III-V heterostructure, whereas As appears only in the QD-like region, substituting the P sites to form $InAs_xP_{1-x}$ with an estimated average composition of x = 0.42. For sample S-1, the composition was found to be x = 0.57. With the results of both STEM and EDS scanning, it is therefore confirmed that the InP/InAsP interfaces are well-defined without crystal defects, forming high-quality heterostructures. InP and InAsP have type-I band alignment, and the emission wavelength of the InAsP QD can be tailored by varying the material composition, as shown in the following sections, which describe the optical measurements and modeling of the electronic QD-type structure.

Optical properties of the InP/InAsP/InP/Si nano-heterostructures

The optical characterization of InP/InAsP/InP/Si nano-heterostructures was carried out in a µPL setup in the range of 5 – 250 K. The laser spot in the µPL experiment of approximately 2 µm thus is expected to excite ~10 nanostructures (refer to Fig. 1c on geometry of the sample). The results of the optical investigation are presented in Fig. 3.

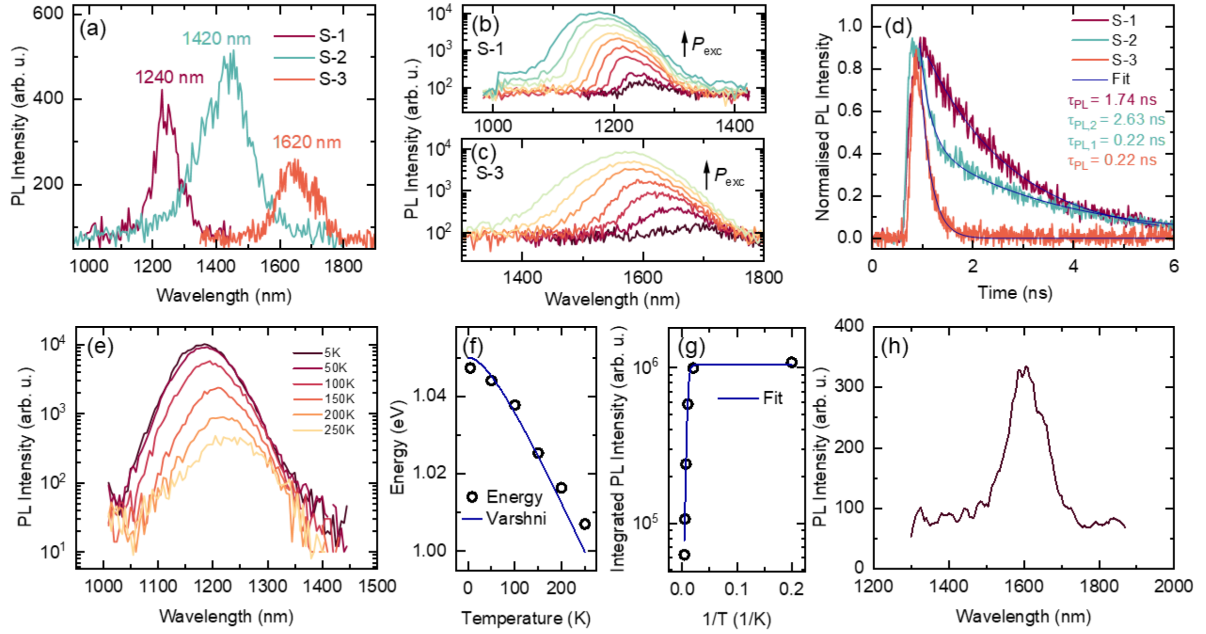

Figure 3. Micro-photoluminescence (µPL) investigation of the QD-like structures at 5K, (a) µPL spectra taken from samples S-1, S-2, and S-3, (b), (c) excitation power dependent µPL spectra for samples (b) S-1, and (c) S-3, (d) time-resolved µPL traces for samples taken at their µPL peak wavelength, (e) temperature-dependent spectra for sample S-1, analyzed in (f) and (g): (f) emission energy overlapped with Varshni bandgap renormalization trend, (g) integrated µPL signal intensity with the Arrhenius fit line, (h) µPL spectrum of a single InP/InAsP/InP/Si structure recorded for sample S-3.

All investigated samples emit in the telecom wavelengths range. The exemplary samples demonstrate optical emission centered at 1240 nm for S-1, at 1420 nm for S-2, and at 1620 nm for S-3. The spectra taken at the 1 mW excitation power are plotted in Fig. 3a. The redshift of the emission wavelength correlates with the amount of arsine supplied during the As/P exchange. The broadening of the PL peaks can be explained by the relatively high laser power needed for optical excitation (at least 20 µW), which increases the higher states occupation probability and thus the full width at half maximum (FWHM) of the PL peak. This behavior is caused by the low spacing of the quantized level for electrons and holes, as described in the following section. Additionally, we expect the broadening due to the spontaneous spectral diffusion originating in the fluctuating electric fields resulting from the accumulation and redistribution of charges either in the vicinity of the InAsP nanostructure or at the InAsP/Si interface states. Consequently, the PL emission exhibits stochastic fluctuations in peak position and linewidth[40]. These fluctuations are thought to primarily influence the linewidth of the emission of single quantum emitters due to the inherent averaging of the emission energy that occurs during the time required to measure a spectrum. Notably, we did not detect the emission related to the defects in the silicon matrix, often observed as a relatively narrow emission line at 1.1 eV (λ = 1125 nm)[41]. This absence supports the interpretation that the observed emission originates from the QD-like structures.

The excitation-power dependent µPL spectra for the nominally 50 nm-large openings from samples S-1 and S-3 are shown in Figs. 3b and 3c. As the laser power changes over

three orders of magnitude from 20 μW to 20 mW, the central energy of the μPL peak shifts by 64 meV for S-1 and 52 meV for S-3. The power-dependent blueshift of the emission energy can be explained by the state-filling effect in the QD-like structures: the finite density of states and the state energy quantization result in the increased probability of carrier population of the excited states. Consequently, the carrier recombination from their excited states to the ground states generates high-energy photons, effectively contributing to the increase of the PL intensity at the high-energy tail of the emission peak.

Subsequently, the time evolution of the μPL signal of InAsP QDs was examined via the time-resolved PL (TRPL) measurements. Figure 3d shows the TRPL traces for all samples, taken at the energy corresponding to the maximum of their PL emission peak. TRPL trace for sample S-1 exhibits a monoexponential decay, which can be fitted with the function $I(t) = Ae^{-t/\tau}$, where A is the scaling factor, and τ is the observed PL decay time, here τ = 1.74 ns, in good agreement with the PL decay times typically observed for the InAs/InP QDs, grown in Stranski-Krastanov[42–44] or droplet epitaxy[45,46] mode, hence confirming the high structural and optical quality of S-1 structure. On the other hand, two decay time constants are needed to fit the TRPL trace for S-2, according to the bi-exponential decay formula $I(t) = Ae^{-t/\tau_1} + Be^{-t/\tau_2}$, with fitted values of τ_1 = 0.22 ns and τ_2 = 2.63 ns. The presence of an additional non-radiative carrier recombination channel can explain the observed modification of the TRPL signal. Among the possible non-radiative channels is the carrier relaxation using the mid-bandgap states, introduced into the InAsP bandgap by the structural defects in the crystal lattice or at the InAsP/Si interface. The TRPL decay time for S-3 is even more dominated by the non-radiative emission, demonstrating a relatively short monoexponential decay with the time constant τ = 0.22 ns. This can indicate the presence of a higher density of structural defects in the active material compared to the S-2 case, most probably resulting from a larger volume of InAsP QD-like structure resulting from an excessively prolonged As/P exchange applied in sample S-3.

The temperature-dependent PL spectra for sample S-1 are shown in Fig. 3e, while this series is analyzed in Figs. 3f-g. The central emission energy follows the Varshni relation:[47]

$$E_g(T) = E_g(0) - \frac{\alpha T^2}{T + \beta}$$

where E_g is the bandgap energy and parameters are taken for InAs, $\alpha = 2.76 \times 10^{-4}$ eV/K, and β = 93 K. The corresponding curve is plotted atop the energies recorded for PL spectra in Fig. 3f. The empirical Varshni formula considers only the thermal change of the semiconductor band gap. The emission intensity decreases above 50 K, and this quench can be described by the Arrhenius formula that considers one activation process of energy E_q and relative rate B_q[48]:

$$I(T) = \frac{I_0}{1 + B_q \exp\left(-E_q/k_B T\right)}$$

The obtained activation energy for the PL intensity quench is E_q = 39 meV. The calculated confinement energy for an exemplary $InAs_{0.45}P_{0.55}$ QD in the InP matrix is ~150 meV for electrons and ~250 meV for holes (see Fig. 4b). Thus, the PL intensity quench cannot be explained by the escape of carriers to the surrounding InP. The carriers might be excited to the mid-gap states introduced by the defects, where they recombine non-radiatively. Alternatively, as the band alignment for holes at the InAsP/Si interface can be of type II[30,49–52], or InAsP can confine the holes very weakly, holes can also escape horizontally from InAsP to the neighboring silicon matrix.

The PL investigation was mainly performed for the nano-heterostructures with a surface density of 5 structures/μm^2. Therefore, the properties are averaged over a few emitters, and the observed broadening of the PL spectrum can result from the homogenous of the emitter ensemble or due to the spectral diffusion on the single-emitter level. In the first scenario, the As/P exchange efficiency depends on the orientation of the exposed InP facets, which are determined by the shape and size of the grown InP seeds. Any variation in this respect can introduce inhomogeneity into the size and composition of QDs within the excitation spot, thus broadening the PL peak.

Nevertheless, the PL investigations on a single emitter level revealed a spectrum (shown in Fig. 3h) with an FWHM of 60 meV, similar to those recorded for the ensemble, favoring the second scenario of the considerable impact of the spectral diffusion on the single-emitter level. The recorded FWHM value is comparable with the emission broadening for, e.g., CdSe/CdS/ZnS single colloidal quantum dots, where the spectral diffusion broadening mechanism was also observed[53]. We conclude that the FWHM of the ensemble PL peak is determined by the PL emission of the individual emitters broadened by spectral diffusion, while the discussed QD inhomogeneity is significantly less important.

Calculations of the electronic structure

We calculated the electronic structure of the $InAs_xP_{1-x}$ QD-like structures in the InP matrix within the eight-band k·p method to investigate the dimensionality of the carrier confinement and the agreement between the expected electron-hole (e-h) recombination energy with the EDS data. We employed the commercially available nextnano software[54] to calculate the single-particle electron states. For this, the continuum elasticity theory is utilized to model the strain distribution, followed by the calculations of the electron eigenstates within the eight-band k·p method, including the strain-driven piezoelectric field. The results of the calculations are shown in Fig. 4.

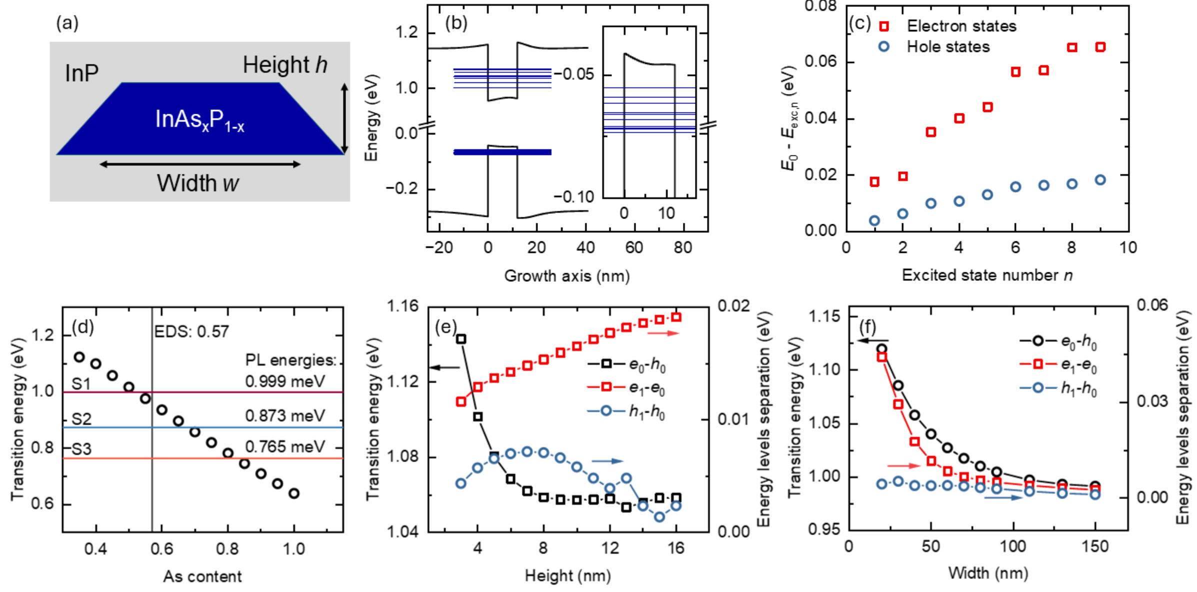

Figure 4. Calculations of the InAsP/InP electronic structure in eight-band k·p. (a) Scheme of the investigated structure, (b) conduction and heavy hole valence bands with electron and hole states confined in the InAsP QD-like structure (inset: close up to the valence band), (c) energy levels separation between the ground state E_0 and consecutive excited states $E_{exc,n}$, (d), (e), (f) transition energy between the ground electron and heavy-hole states e_0-h_0 (black datapoints) as a function of (d) As content in the nanostructure, overlaid with the PL peak energies for all three samples, and the EDS composition of x = 0.57 for S-1 indicated by the vertical line, (e) nanostructure's height, and (f) its width. In panels (e) and (f), the right axis is used to show the separation between the ground and first excited states for electrons (e_1-e_0, red squares) and holes (h_1-h_0, blue circles).

Fig. 4a shows the scheme of the simulated structure, with the geometry based on the STEM image shown in Fig. 2. We model the nanostructure as an in-plane symmetric $InAs_xP_{1-x}$ truncated pyramid inserted in the InP matrix. We assume the wall inclination angle of 45 °, though it is impossible to infer the full 3D model of the $InAs_xP_{1-x}$ from the limited number of STEM images and the inherently destructive nature of the STEM experiments. However, this is unnecessary, as our motivation is to describe the general trends. We take the dimensions and composition of the nano-heterostructure as determined in the scans shown in Fig. 2: height of 12 nm, width of 40 nm, and the As content of x = 0.45, though width and height are expected to vary slightly across the ensemble of openings.

The conduction and heavy-hole valence bands taken along the growth axis at the center of the structure are shown in Fig. 4b, together with energies of the first 9 hole and 9 electron confined states. The pronounced energy difference between the ground states and the respective $InAs_{0.45}P_{0.55}$ band edges, together with the discrete state energy ladders, evidence the quantum confinement in the nanostructures. Supplementary Figure 2 shows the calculated probability distributions for ground and first excited states. Figure 4c shows the energy difference between the ground and consecutive excited states for holes and electrons. The relatively dense energy ladders for electron and hole states support the interpretation that in the regime of high excitation power, many excited states have a relatively high occupation probability, broadening the PL spectrum.

We define the transition energy as the difference between the ground state levels for electrons and holes, e_0-h_0, and show its dependence on the As content in Fig. 4d, on height in Fig. 4e, and on width in Fig. 4e. All parameters influence the transition energy, with As content having the largest influence (energy change from 1.13 eV to 0.63 eV when the As composition is increased from 35 % to 100 %). We found that at least 35 % of As in the nanostructure is required to confine both carriers in the InAsP potential. The expected transition energy for the InAsP nanostructures with As content of x = 0.57 (sample S-1) is 0.96 eV, which is in close agreement with the central PL energy of 0.99 eV, recorded for the same sample.

Based on the calculations of the energy levels for different heights, shown in Fig. 4e, the quantum size effect along the growth direction is most pronounced in the structures thinner than 10 nm, though the quantization energy (the energy difference between the first excited state and the ground state) in both bands depends on the size in the entire investigated range of 3-16 nm. We note that the InAsP nanostructure's height of 12 nm, as determined by the STEM, can be easily overestimated due to the imperfect lamella's orientation compared to the assumed one (parallel to the growth direction). The lamella's tilt during the STEM scanning can introduce the artificial thickening of the InAsP layer.

Importantly, the three-dimensional confinement of carriers can be confirmed by the evolution of the calculated energies for varying InAsP width, plotted in Fig. 4f. The quantum size effect can be observed as a change in the transition energy occurring for nanostructures narrower than 110 nm. Based on the changes in the quantization energies for electrons and holes (right axis in Fig. 4f), we can conclude that the electron states ladder is much more affected by the change of the in-plane size of the nanostructure due to its weaker confinement (see Fig. 4b). The calculated changes in the transition and the quantization energies for the width range realized in investigated nanostructures confirm the existence of the in-plane quantum confinement, and in consequence, of the three-dimensional quantum confinement. This observation further supports terming the InAsP nanostructures as 'quantum dot-like' structures.

Conclusions

In conclusion, we demonstrated the monolithic integration of the InAsP/InP nano-heterostructures on silicon. The nano-heterostructures are grown in the pyramidal openings defined by the {111} planes of the (100)-oriented silicon substrate. The positions of the nanostructures are predetermined by the e-beam lithography and selective anisotropic wet etching of silicon. The systematic investigation of the morphology, chemical composition, and optical properties of the nano-heterostructures allowed the evaluation of their geometry and revealed their QD-like behavior. Moreover, the eight-band k·p calculations based on morphological studies prove the energy levels' quantization in three spatial dimensions. However, the unoptimized cap geometry prevents efficient signal collection during optical measurements. Therefore, the applied high excitation power significantly broadened the optical response of the nanostructures.

We demonstrate that we can engineer the emission wavelengths on demand across the entire telecom range by tailoring growth parameters. Our results show great potential for fabricating light sources grown directly on silicon and emitting at various wavelengths covering the telecom range for diverse optical and silicon photonic-based applications, such as CMOS-compatible energy-efficient nanolasers or nanoLED with a nanometer-scale active region. Future optimization should focus on engineering the photonic environment of the nano-heterostructures to increase the light outcoupling efficiency.

Methods

Substrate preparation

Samples were prepared by starting with an undoped Si (001) wafer, on which 23 nm-thick Si_3N_4 was deposited by LPCVD. The wafer was patterned using e-beam lithography in a JEOL JBX-9500FSZ e-beam writer using the 100 kV acceleration voltage and CSAR (AR-6200.09) resist. After developing in ZED N-50 for 1 min, the Si_3N_4 was dry etched in ICP-RIE using CHF_3/CH_4 chemistry. Oxygen plasma ashing was used to strip the resist, followed by KOH etching to form inverted pyramids in silicon at 70 °C. Piranha cleaning was performed before dipping the sample for 3 mins into a buffered HF solution and immediately loading it into the MOVPE chamber to prevent oxidation of the silicon surface.

Epitaxial growth

The growth is carried out in an MOVPE reactor (Emcore D-125 Turbo-disc) at 60 Torr (1000 rpm) using hydrogen as the carrier gas. TMIn, PH_3, and AsH_3 are used as precursors for In, P, and As, respectively. First, the surface preparation is performed at 750 °C under the high AsH_3 flux. Then, the temperature is ramped down to the growth temperature of 600 °C, and TMIn and PH_3 were simultaneously turned on to start the InP growth. Then, InAsP nanostructures are formed by shutting off TMIn and cooling down to the exchange temperature of 510 °C under TBP flow, followed by turning on AsH_3, and simultaneously turning off TBP flows. For the growth of the InP cap layer, the temperature is kept at 510 °C. After the growth, the reactor is cooled down with TBP flow to prevent the desorption of the cap layer.

Optical characterization

The samples with the nano-heterostructures were held in a helium-flow cryostat, allowing for control of the sample temperature in the range of 4.2-300 K. For the standard μPL studies, the structures were optically excited through a microscope objective with NA = 0.4 and 20× magnification using 640 nm or 805 nm light generated with semiconductor laser diodes. The same objective was used to collect the μPL signal and to direct it for spectral analysis into a 0.32 m-focal-length monochromator equipped with a 600 grooves/mm diffraction grating and a liquid-nitrogen-cooled InGaAs multichannel array detector, providing spatial and spectral resolution of about 2 μm and 100 μeV, respectively.

The time-resolved μPL was measured in the same setup. Here, the nanostructures were excited by 50 ps-long pulses with a repetition rate of 80 MHz and a central wavelength of 805 nm. At the same time, the second monochromator output port was equipped with the fiber coupling system, transmitting the signal to an NbN-based SNSPD (Scontel) with above 50 % quantum efficiency in the range of 1.2-1.6 μm and 100 dark counts per second. A multichannel picosecond event timer (PicoHarp 300 by PicoQuant GmbH) analyzed the single photon counts as a time-to-amplitude converter. The overall time resolution of the setup is estimated to be 80 ps.

Lamella preparation

The lamellae were prepared with a plasma-focused ion beam scanning electron microscope (plasma FIB-SEM, Thermo Fisher's Helios 5 Hydra Ux DualBeam). SEM images were acquired with accelerating voltages between 2 kV-5 kV and electron currents between 100 pA-200 pA. Secondary electrons were used as signal. The field-free mode was chosen for sample navigation, while for high-quality imaging the immersion mode was applied. Xe ions were used for sample navigation with the ion beam (accelerating voltage: 30 kV, ion current: 10 pA). The electron beam was used to deposit a thin layer of carbon followed by a slightly thicker layer of a carbon/platinum mixture (accelerating voltage: 2 kV, electron current: 1.6 nA). Subsequently, a thick layer of a carbon/platinum mixture was deposited by the ion beam (accelerating voltage: 12 kV, ion current: 1 nA).

The lamellae were prepared by milling trenches (regular cross-section, accelerating voltage: 30 kV, ion current: 60 nA), followed by cleaning the surfaces (cleaning cross-section, accelerating voltage: 30 kV, ion current: 40 nA) and a J-cut (accelerating voltage: 30 kV, ion current: 15 nA). After a final cleaning of the surfaces, the lamellae were attached to a needle (Pt/C, accelerating voltage: 30 kV, ion current: 100 pA), the remaining bridge was cut (accelerating voltage: 30 kV, ion current: 1 nA), and the structure was lifted out of the substrate. Finally, the lamellae were attached to a TEM grid suitable for electron microscopy investigations, followed by precise thinning (Xe, accelerating voltage: 30 kV, ion current: 200 pA) and polishing steps (Ar, accelerating voltage: 5 kV/2 kV, ion current: 61 pA/25 pA) to make the quantum dots accessible for STEM measurements.

Electron microscopy

A probe and image-corrected state-of-the-art electron microscope (Thermo Fisher's Ultra Spectra STEM) were used for the study. The microscope is equipped with an Ultra-X EDS system for the efficient collection of EDS data. HAADF STEM images were acquired with an accelerating voltage of 300 kV after probe correction with convergence angles between 30 mrad and 18.5 mrad and a camera length of 109 mm.

Acknowledgments

We acknowledge financial support from the Danish National Research Foundation through NanoPhoton - Center for Nanophotonics, grant number DNRF147, and the National Science Centre in Poland within grant No. 2019/33/B/ST5/02941.

References

[1] Zhou, Z., Yin, B. and Michel, J., “On-chip light sources for silicon photonics,” Light Sci Appl **4**(11) (2015).

[2] Liu, S., Liu, A., Bowers, J. E., Wan, Y. and Norman, J., “Quantum Dot Lasers and Amplifiers on Silicon: Recent Advances and Future Developments,” IEEE Nanotechnol Mag **15**(2) (2021).

[3] Fang, A. W., Park, H., Cohen, O., Jones, R., Paniccia, M. J. and Bowers, J. E., “Electrically pumped hybrid AlGaInAs-silicon evanescent laser,” Opt Express **14**(20) (2006).

[4] Park, H., Fang, A. W., Liang, D., Kuo, Y. H., Chang, H. H., Koch, B. R., Chen, H. W., Sysak, M. N., Jones, R. and Bowers, J. E., “Photonic integration on the hybrid silicon evanescent device platform,” Advances in Optical Technologies (2008).

[5] Komljenovic, T., Davenport, M., Hulme, J., Liu, A. Y., Santis, C. T., Spott, A., Srinivasan, S., Stanton, E. J., Zhang, C. and Bowers, J. E., “Heterogeneous silicon photonic integrated circuits,” Journal of Lightwave Technology **34**(1) (2016).

[6] Liang, D., Huang, X., Kurczveil, G., Fiorentino, M. and Beausoleil, R. G., “Integrated finely tunable microring laser on silicon,” Nat Photonics **10**(11) (2016).

[7] Shu, H., Chang, L., Tao, Y., Shen, B., Xie, W., Jin, M., Netherton, A., Tao, Z., Zhang, X., Chen, R., Bai, B., Qin, J., Yu, S., Wang, X. and Bowers, J. E., “Microcomb-driven silicon photonic systems,” Nature **605**(7910) (2022).

[8] Shang, C., Wan, Y., Selvidge, J., Hughes, E., Herrick, R., Mukherjee, K., Duan, J., Grillot, F., Chow, W. W. and Bowers, J. E., “Perspectives on Advances in Quantum Dot Lasers and Integration with Si Photonic Integrated Circuits,” ACS Photonics **8**(9) (2021).

[9] Tang, M., Chen, S., Wu, J., Jiang, Q., Kennedy, K., Jurczak, P., Liao, M., Beanland, R., Seeds, A. and Liu, H., “Optimizations of defect filter layers for 1.3-μm InAs/GaAs quantum-dot lasers monolithically grown on Si substrates,” IEEE Journal of Selected Topics in Quantum Electronics **22**(6) (2016).

[10] Chen, S., Li, W., Wu, J., Jiang, Q., Tang, M., Shutts, S., Elliott, S. N., Sobiesierski, A., Seeds, A. J., Ross, I., Smowton, P. M. and Liu, H., “Electrically pumped continuous-wave III-V quantum dot lasers on silicon,” Nat Photonics **10**(5) (2016).

[11] Norman, J., Kennedy, M. J., Selvidge, J., Li, Q., Wan, Y., Liu, A. Y., Callahan, P. G., Echlin, M. P., Pollock, T. M., Lau, K. M., Gossard, A. C. and Bowers, J. E., “Electrically pumped continuous wave quantum dot lasers epitaxially grown on patterned, on-axis (001) Si,” Opt Express **25**(4) (2017).

[12] Kwoen, J., Jang, B., Lee, J., Kageyama, T., Watanabe, K. and Arakawa, Y., "All MBE grown InAs/GaAs quantum dot lasers on on-axis Si (001)," Opt Express **26**(9) (2018).

[13] Zhang, B., Wei, W. Q., Wang, J. H., Wang, H. L., Zhao, Z., Liu, L., Cong, H., Feng, Q., Liu, H., Wang, T. and Zhang, J. J., "O-band InAs/GaAs quantum-dot microcavity laser on Si (001) hollow substrate by in-situ hybrid epitaxy," AIP Adv **9**(1) (2019).

[14] Wan, Y., Zhang, S., Norman, J., Kennedy, M. J., He, W., Tong, Y., Shang, C., He, J. J., Tsang, H. K., Gossard, A. C. and Bowers, J. E., "1.3 μm Tunable Quantum Dot Lasers," Conference Proceedings - Lasers and Electro-Optics Society Annual Meeting-LEOS **2020-May** (2020).

[15] Shang, C., Hughes, E., Wan, Y., Dumont, M., Koscica, R., Selvidge, J., Herrick, R., Gossard, A. C., Mukherjee, K. and Bowers, J. E., "High-temperature reliable quantum-dot lasers on Si with misfit and threading dislocation filters," Optica **8**(5) (2021).

[16] Dhingra, P., Su, P., Li, B. D., Hool, R. D., Muhowski, A. J., Kim, M., Wasserman, D., Dallesasse, J. and Lee, M. L., "Low-threshold InP quantum dot and InGaP quantum well visible lasers on silicon (001)," Optica **8**(11) (2021).

[17] Limame, I., Ludewig, P., Shih, C.-W., Hohn, M., Palekar, C. C., Stolz, W. and Reitzenstein, S., "High-quality single InGaAs/GaAs quantum dot growth on a silicon substrate for quantum photonic applications," Optica Quantum **2**(2), 117–123 (2024).

[18] Wan, Y., Norman, J. C., Tong, Y., Kennedy, M. J., He, W., Selvidge, J., Shang, C., Dumont, M., Malik, A., Tsang, H. K., Gossard, A. C. and Bowers, J. E., "1.3 μm Quantum Dot-Distributed Feedback Lasers Directly Grown on (001) Si," Laser Photon Rev **14**(7) (2020).

[19] Wan, Y., Zhang, S., Norman, J. C., Kennedy, M. J., He, W., Liu, S., Xiang, C., Shang, C., He, J.-J., Gossard, A. C. and Bowers, J. E., "Tunable quantum dot lasers grown directly on silicon," Optica **6**(11) (2019).

[20] Luxmoore, I. J., Toro, R., Pozo-Zamudio, O. Del, Wasley, N. A., Chekhovich, E. A., Sanchez, A. M., Beanland, R., Fox, A. M., Skolnick, M. S., Liu, H. Y. and Tartakovskii, A. I., "III-V quantum light source and cavity-QED on silicon," Sci Rep **3** (2013).

[21] Borg, M., Schmid, H., Moselund, K. E., Signorello, G., Gignac, L., Bruley, J., Breslin, C., Das Kanungo, P., Werner, P. and Riel, H., "Vertical III-V nanowire device integration on Si(100)," Nano Lett **14**(4) (2014).

[22] Mauthe, S., Triviño, N. V., Baumgartner, Y., Sousa, M., Caimi, D., Stöferle, T., Schmid, H. and Moselund, K. E., "InP-on-Si Optically Pumped Microdisk Lasers via Monolithic Growth and Wafer Bonding," IEEE Journal of Selected Topics in Quantum Electronics **25**(6) (2019).

[23] Merckling, C., Waldron, N., Jiang, S., Guo, W., Barla, K., Heyns, M., Collaert, N., Thean, A. and Vandervorst, W., "(Invited) Selective-Area Metal Organic Vapor-Phase Epitaxy of III-V on Si: What About Defect Density?," ECS Trans **64**(6) (2014).

[24] Wang, Z., Tian, B., Pantouvaki, M., Guo, W., Absil, P., Van Campenhout, J., Merckling, C. and Van Thourhout, D., “Room-temperature InP distributed feedback laser array directly grown on silicon,” Nat Photonics **9**(12) (2015).

[25] Niu, G., Capellini, G., Hatami, F., Di Bartolomeo, A., Niermann, T., Hussein, E. H., Schubert, M. A., Krause, H. M., Zaumseil, P., Skibitzki, O., Lupina, G., Masselink, W. T., Lehmann, M., Xie, Y. H. and Schroeder, T., “Selective Epitaxy of InP on Si and Rectification in Graphene/InP/Si Hybrid Structure,” ACS Appl Mater Interfaces **8**(40) (2016).

[26] Iemmo, L., Di Bartolomeo, A., Giubileo, F., Luongo, G., Passacantando, M., Niu, G., Hatami, F., Skibitzki, O. and Schroeder, T., “Graphene enhanced field emission from InP nanocrystals,” Nanotechnology **28**(49) (2017).

[27] Vukajlovic-Plestina, J., Kim, W., Ghisalberti, L., Varnavides, G., Tütüncuoglu, G., Potts, H., Friedl, M., Güniat, L., Carter, W. C., Dubrovskii, V. G. and Fontcuberta i Morral, A., “Fundamental aspects to localize self-catalyzed III-V nanowires on silicon,” Nat Commun **10**(1) (2019).

[28] Bollani, M., Bietti, S., Frigeri, C., Chrastina, D., Reyes, K., Smereka, P., Millunchick, J. M., Vanacore, G. M., Burghammer, M., Tagliaferri, A. and Sanguinetti, S., “Ordered arrays of embedded Ga nanoparticles on patterned silicon substrates,” Nanotechnology **25**(20) (2014).

[29] Oehler, F., Cattoni, A., Scaccabarozzi, A., Patriarche, G., Glas, F. and Harmand, J. C., “Measuring and Modeling the Growth Dynamics of Self-Catalyzed GaP Nanowire Arrays,” Nano Lett **18**(2) (2018).

[30] Viazmitinov, D. V., Berdnikov, Y., Kadkhodazadeh, S., Dragunova, A., Sibirev, N., Kryzhanovskaya, N., Radko, I., Huck, A., Yvind, K. and Semenova, E., “Monolithic integration of InP on Si by molten alloy driven selective area epitaxial growth,” Nanoscale **12**(46) (2020).

[31] Wei, W. Q., He, A., Yang, B., Wang, Z. H., Huang, J. Z., Han, D., Ming, M., Guo, X., Su, Y., Zhang, J. J. and Wang, T., “Monolithic integration of embedded III-V lasers on SOI,” Light Sci Appl **12**(1) (2023).

[32] Herranz, J., Corfdir, P., Luna, E., Jahn, U., Lewis, R. B., Schrottke, L., Lähnemann, J., Tahraoui, A., Trampert, A., Brandt, O. and Geelhaar, L., “Coaxial GaAs/(In,Ga)As Dot-in-a-Well Nanowire Heterostructures for Electrically Driven Infrared Light Generation on Si in the Telecommunication O Band,” ACS Appl Nano Mater **3**(1) (2020).

[33] De Koninck, Y., Caer, C., Yudistira, D., Baryshnikova, M., Sar, H., Hsieh, P.-Y., Patra, S. K., Kuznetsova, N., Colucci, D., Milenin, A., Yimam, A. A., Morthier, G., Thourhout, D. Van, Verheyen, P., Pantouvaki, M., Kunert, B. and Van Campenhout, J., “GaAs nano-ridge laser diodes fully fabricated in a 300 mm CMOS pilot line.”

[34] Kunert, B., Mols, Y., Baryshniskova, M., Waldron, N., Schulze, A. and Langer, R., “How to control defect formation in monolithic III/V hetero-epitaxy on (100) Si? A critical review on current approaches,” Semicond Sci Technol **33**(9) (2018).

[35] Kunert, B., Guo, W., Mols, Y., Tian, B., Wang, Z., Shi, Y., Van Thourhout, D., Pantouvaki, M., Van Campenhout, J., Langer, R. and Barla, K., "III/V nano ridge structures for optical applications on patterned 300 mm silicon substrate," Appl Phys Lett **109**(9) (2016).

[36] Güniat, L., Caroff, P. and Fontcuberta I Morral, A., "Vapor Phase Growth of Semiconductor Nanowires: Key Developments and Open Questions," Chem Rev **119**(15) (2019).

[37] Tauchnitz, T., Berdnikov, Y., Dubrovskii, V. G., Schneider, H., Helm, M. and Dimakis, E., "A simple route to synchronized nucleation of self-catalyzed GaAs nanowires on silicon for sub-Poissonian length distributions," Nanotechnology **29**(50) (2018).

[38] Pozuelo, M., Zhou, H., Lin, S., Lipman, S. A., Goorsky, M. S., Hicks, R. F. and Kodambaka, S., "Self-catalyzed growth of InP/InSb axial nanowire heterostructures," J Cryst Growth **329**(1) (2011).

[39] Kappelt, M., Türck, V., Bimberg, D., Kirmse, H., Hähnert, I. and Neumann, W., "InGaAs and InAsP V-groove quantum wires using arsenic/phosphorus exchange preparation," J Cryst Growth **195**(1–4) (1998).

[40] Empedocles, S. A. and Bawendi, M. G., "Influence of spectral diffusion on the line shapes of single CdSe nanocrystallite quantum dots," Journal of Physical Chemistry B **103**(11) (1999).

[41] Nguyen, H. T., Rougieux, F. E., Yan, D., Wan, Y., Mokkapati, S., De Nicolas, S. M., Seif, J. P., De Wolf, S. and MacDonald, D., "Characterizing amorphous silicon, silicon nitride, and diffused layers in crystalline siliconsolarcellsusingmicro-photoluminescence spectroscopy," Solar Energy Materials and Solar Cells **145**, 403–411 (2016).

[42] Takemoto, K., Takatsu, M., Hirose, S., Yokoyama, N., Sakuma, Y., Usuki, T., Miyazawa, T. and Arakawa, Y., "An optical horn structure for single-photon source using quantum dots at telecommunication wavelength," J Appl Phys **101**(8) (2007).

[43] Musiał, A., Holewa, P., Wyborski, P., Syperek, M., Kors, A., Reithmaier, J. P., Sęk, G. and Benyoucef, M., "High-Purity Triggered Single-Photon Emission from Symmetric Single InAs/InP Quantum Dots around the Telecom C-Band Window," Adv Quantum Technol **3**(2) (2020).

[44] Holewa, P., Vajner, D. A., Zięba-Ostój, E., Wasiluk, M., Gaál, B., Sakanas, A., Burakowski, M., Mrowiński, P., Krajnik, B., Xiong, M., Yvind, K., Gregersen, N., Musiał, A., Huck, A., Heindel, T., Syperek, M. and Semenova, E., "High-throughput quantum photonic devices emitting indistinguishable photons in the telecom C-band," Nat Commun **15**(1), 3358 (2024).

[45] Phillips, C. L., Brash, A. J., Godsland, M., Martin, N. J., Foster, A., Tomlinson, A., Dost, R., Babazadeh, N., Sala, E. M., Wilson, L., Heffernan, J., Skolnick, M. S. and Fox, A. M., "Purcell-enhanced single photons at telecom wavelengths from a quantum dot in a photonic crystal cavity," Sci Rep **14**(1) (2024).

[46] Holewa, P., Kadkhodazadeh, S., Gawełczyk, M., Baluta, P., Musiał, A., Dubrovskii, V. G., Syperek, M. and Semenova, E., "Droplet epitaxy symmetric InAs/InP

quantum dots for quantum emission in the third telecom window: morphology, optical and electronic properties," Nanophotonics **11**(8) (2022).

[47] Varshni, Y. P., "Temperature dependence of the energy gap in semiconductors," Physica **34**(1), 149–154 (1967).

[48] Lambkin, J. D., Dunstan, D. J., Homewood, K. P., Howard, L. K. and Emeny, M. T., "Thermal quenching of the photoluminescence of InGaAs/GaAs and InGaAs/AlGaAs strained-layer quantum wells," Appl Phys Lett **57**(19), 1986–1988 (1990).

[49] Bru-Chevallier, C., El Akra, A., Pelloux-Gervais, D., Dumont, H., Canut, B., Chauvin, N., Regreny, P., Gendry, M., Patriarche, G., Jancu, J. M., Even, J., Noe, P., Calvo, V. and Salem, B., "InGaAs quantum dots grown by molecular beam epitaxy for light emission on Si substrates," J Nanosci Nanotechnol **11**(10) (2011).

[50] Heitz, R., Ledentsov, N. N., Bimberg, D., Egorov, A. Y., Maximov, M. V., Ustinov, V. M., Zhukov, A. E., Alferov, Z. I., Cirlin, G. E., Soshnikov, I. P., Zakharov, N. D., Werner, P. and Gösele, U., "Optical properties of InAs quantum dots in a Si matrix," Physica E Low Dimens Syst Nanostruct **7**(3) (2000).

[51] Van De Walle, C. G., "Band lineups and deformation potentials in the model-solid theory," Phys Rev B **39**(3) (1989).

[52] Halder, N. N., Kundu, S., Mukherjee, R., Biswas, D. and Banerji, P., "Catalyst-free direct growth of InP quantum dots on Si by MOCVD: A step toward monolithic integration," Journal of Nanoparticle Research **14**(12) (2012).

[53] Gómez, D. E., Van Embden, J. and Mulvaney, P., "Spectral diffusion of single semiconductor nanocrystals: The influence of the dielectric environment," Appl Phys Lett **88**(15) (2006).

[54] Birner, S., Zibold, T., Andlauer, T., Kubis, T., Sabathil, M., Trellakis, A. and Vogl, P., "Nextnano: General purpose 3-D simulations," IEEE Trans Electron Devices **54**(9) (2007).

Supplementary Information

Engineering Efficient Light Sources for Silicon Photonics: III-V Nano-heterostructures Monolithically Grown on Silicon

Alisha Nanwani[1,2,*], Paweł Wyborski[1,3], Michael S. Seifner[2,4], Shima Kadkhodazadeh[2,4], Grzegorz Sęk[3], Paweł Holewa[1,2,3,**], Kresten Yvind[1,2], Elizaveta Semenova[1,2]

[1]Department of Electrical and Photonics Engineering, Technical University of Denmark, Denmark

[2]Nanophoton- Centre for Nanophotonics, Technical University of Denmark, Denmark

[3]Department of Experimental Physics, Faculty of Fundamental Problems of Technology, Wroclaw University of Science and Technology, 50-370 Wroclaw, Poland

[4]DTU Nanolab, Technical University of Denmark, Denmark

*atana@dtu.dk, **pawhol@dtu.dk

S1 EDS Analysis for samples S-1 and S-3

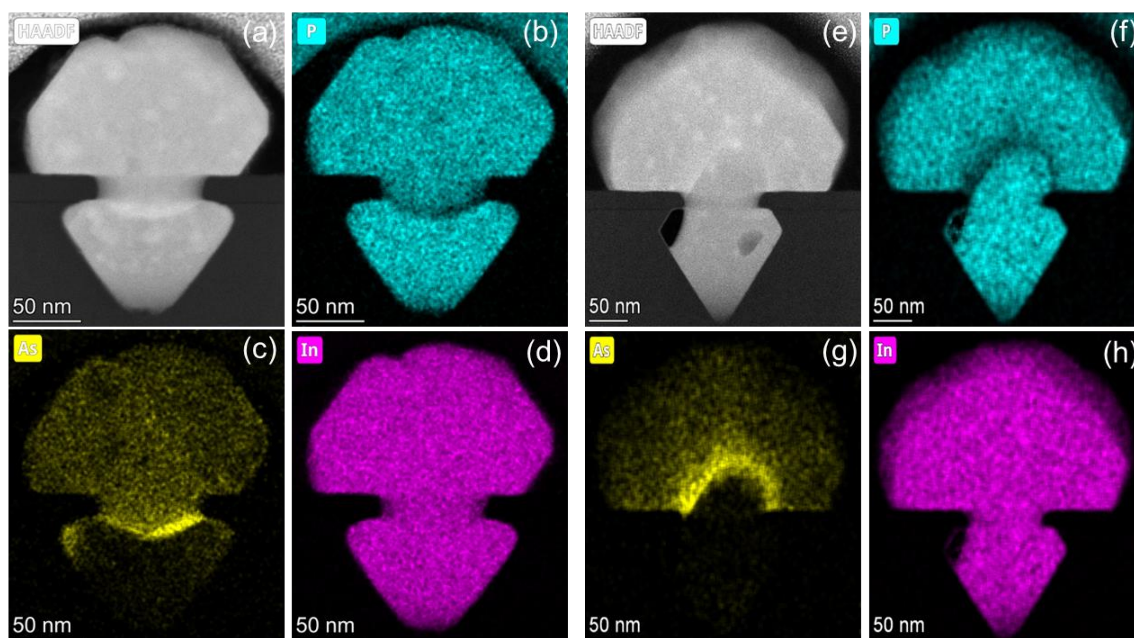

Supplementary Figure S1. EDS analysis of InAsP/InP nano-heterostructures, S-1 (left) and S-3 (right): (a) HAADF-STEM image for S-1, and (b-d) 2D elemental mapping of S-1 (b) P (cyan), (c) As (yellow) and (d) In (magenta), respectively. (e) HAADF-STEM image for S-3, and (f-h) 2D elemental mapping of S-3 (f) P (cyan), (g) As (yellow) and (h) In (magenta), respectively.

S2 Calculated probability distributions

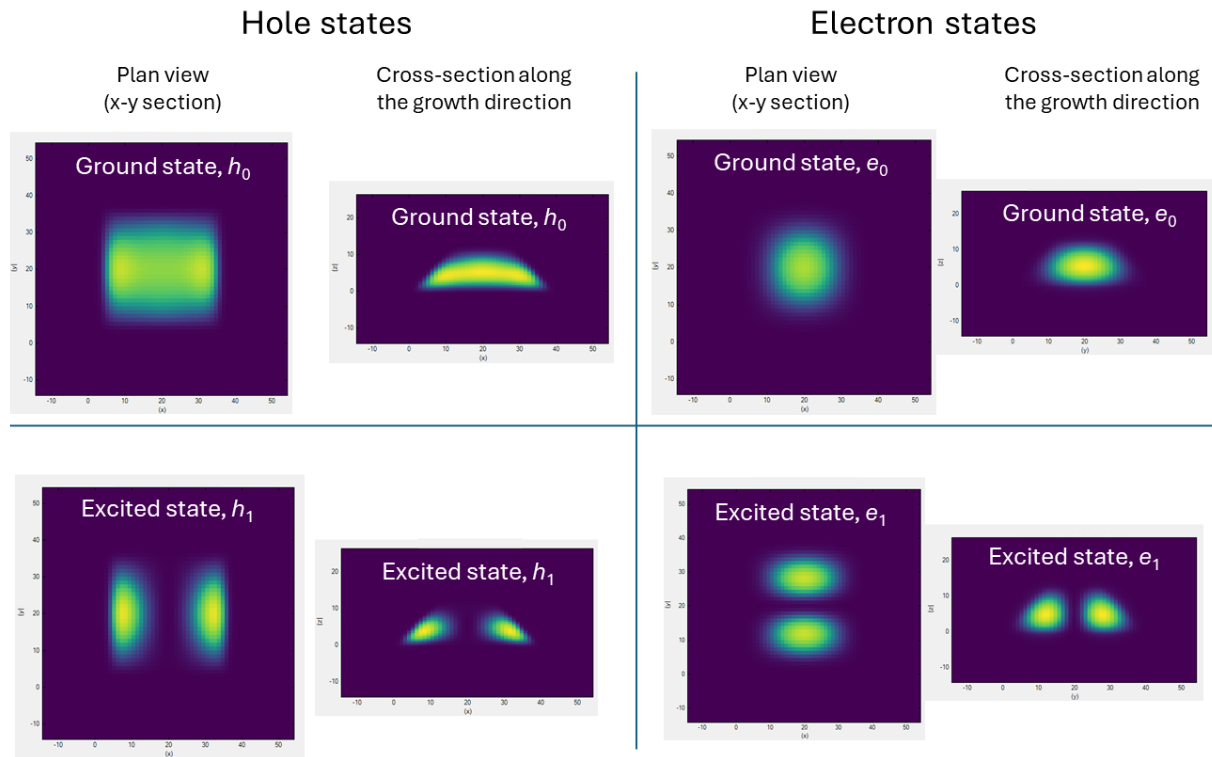

Supplementary Figure S2. Calculated probability distributions for the hole (h, left) and electron (e, right) states: ground (top row, e_0, h_0) and the first excited state (bottom row, e_1, h_1), for the $InAs_{0.45}P_{0.55}$/InP nano-heterostructure.

S3 EDS line scans for sample S-2

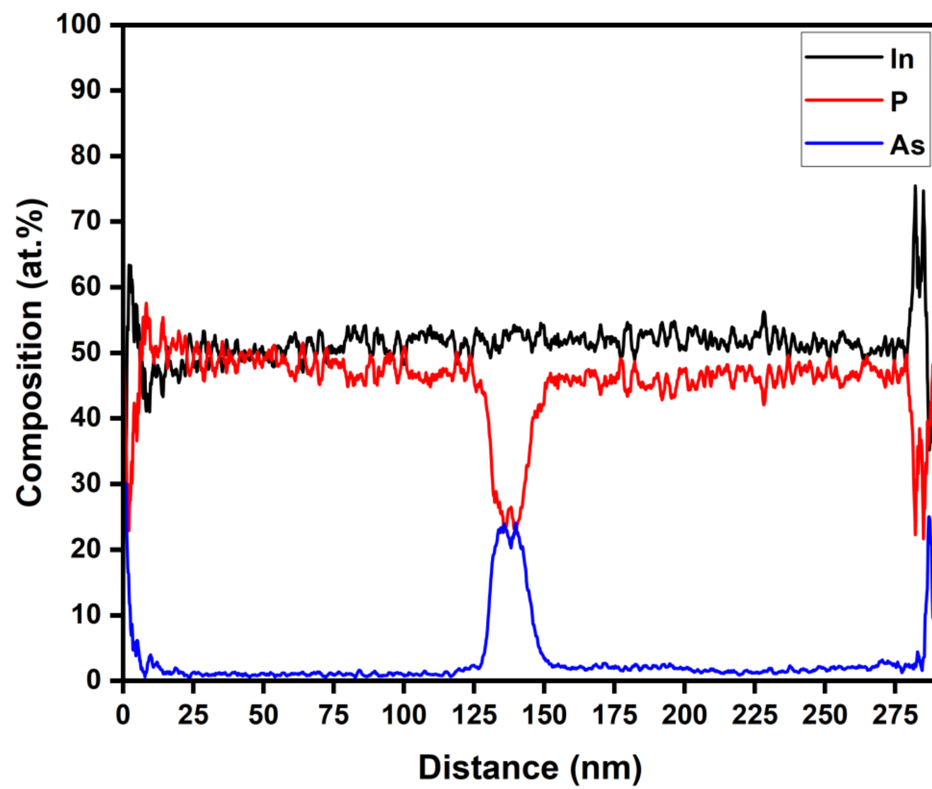

Supplementary Figure S3. 1D line scans by EDS showing the atomic concentration of elements As, P, In, in the heterostructure along the growth direction.